ANALYSIS OF COHESIVE CRACK GROWTH BY THE ELEMENT-FREE GALERKIN METHOD

P. Soparat * **P. Nanakorn** **

School of Civil Engineering and Technology
Sirindhorn International Institute of Technology, Thammasat University
P.O. Box 22, Thammasat-Rangsit Post Office, Pathumthani 12121, Thailand

ABSTRACT

In this study, the element-free Galerkin (EFG) method is extended to include nonlinear behavior of cohesive cracks in 2D domains. A cohesive curved crack is modeled by using several straight-line interface elements connected to form the crack. The constitutive law of cohesive cracks is considered through the use of these interface elements. The stiffness equation of the domain is constructed by directly including, in the weak form of the global system equation, a term related to the energy dissipation along the interface elements. The constitutive law of cohesive cracks can then be considered directly and efficiently by using this energy term. The validity and efficiency of the proposed method are discussed by using problems found in the literature. The proposed method is found to be an efficient method for simulating propagation of cohesive cracks.

Keywords : Element-free Galerkin method, Meshless methods, Cohesive cracks, Cracks in concrete.

1. INTRODUCTION

The finite element method (FEM) has been widely used to perform analysis of 2D cohesive crack propagation [1-6]. Nevertheless, crack analysis using FEM faces several problems. The most serious one is the representation of discontinuities due to cracks. The use of elements in FEM creates difficulties in the treatment of discontinuities that do not coincide with the original mesh lines. One of the traditional techniques for handling these complications is to remesh the domain of the problem in each step of the evolution in such a way that the mesh lines remain coincident with the discontinuities throughout the evolution of the problem [1,4,6]. For this purpose, several complex and robust remeshing algorithms have been developed [4,6]. These algorithms can be computationally more expensive than the assembly and solution processes. Another popular technique is to embed the discontinuities directly into elements and modify the stiffnesses of the elements to incorporate the discontinuities [7-9]. The method is convenient because the modification can be performed at the element level. However, with this technique, it is difficult to maintain the continuity of the crack line. As a result, the continuity of the crack line is mostly neglected. In addition, a spurious mode can also occur if the position and orientation of a crack are freely allowed within the element.

Recently, a new method known as the element-free Galerkin (EFG) method, proposed by Belytschko *et al.* [10], has been developed for solving mechanical problems. Defined by Lancaster and Salkauskas [11], the moving least-square (MLS) approximation which originated in scattered data fitting is chosen to construct EFG shape functions and their derivatives. The core concept of the EFG method is that there is no longer a finite element mesh. Only nodal data and boundary descriptions are required to formulate the discrete Galerkin equations. A background-cell structure, which is independent of nodal points, is employed for the procedure to compute the integral expression. Since the method requires no element, it is an excellent choice for solving crack propagation problems. With the EFG method, a growing crack can be modeled simply by extending the surfaces that correspond to the crack without the need for remeshing. The concept of extending surfaces within the domain to represent crack propagation is actually similar to the treatment of cracks in the boundary element method [12-16]. Several extensions of the EFG method to model crack propagation have been proposed [17-28]. However, all of these works are related to brittle cracks with no traction force between crack surfaces. It is commonly accepted that the linear elastic fracture mechanics (LEFM) is not directly applicable to quasi-brittle materials such as concrete, rock, and ceramics due to a large nonlinear fracture process zone ahead of a crack tip. In the fracture process zone, various microevents, such as microcracking, crack deflection, crack branching, bridging, *etc*., occur and energy is dissipated. The fracture process zone may be represented by integrating the effects from

* Graduate student ** Associate Professor

all the mechanisms within the zone into a fictitious crack ahead of the actual crack as in the fictitious crack model [29]. Across the surfaces of the fictitious crack, cohesive stresses are assumed to be transmitted. In the fictitious crack model, the relationships between these transmitted stresses and the crack opening and sliding displacements are considered as material properties. When mode I cracking is dominant, it is sufficient to consider only the transmitted tensile stress. In this case, the relationship between the transmitted tensile stress and the crack opening displacement is required. Even with the aforementioned difficulties intrinsic to the use of FEM in modeling crack problems, the implementation of the fictitious crack model using FEM has been investigated by many researchers [1-6]. The EFG method has been used to simulate dynamic crack growth in concrete by Belytschko *et al.* [30]. In their proposed method, a crack is represented by a piecewise linear line. Cohesive cracks are not directly included in the weak form of the system equation. Instead, to simulate a cohesive crack, the transmitted tensile stress on the crack surfaces is computed from the current crack opening displacement. The obtained stress is then directly applied to the crack surfaces for the subsequent step of the calculation. In some respects, the basic model for traction-free cracks in the EFG method [18-20] is used for cohesive cracks without any modification. The cohesion effect on crack surfaces is in fact obtained by direct application of the transmitted tensile stress on the crack surfaces.

In this paper, the application of the EFG method for analysis of cohesive crack growth in 2D domains is presented. A cohesive curved crack is model by using straight-line interface elements connected to form the crack. As a result, the crack is represented by a piecewise linear line. These interface elements permit the constitutive law of cohesive cracks to be considered efficiently. In this study, the analysis is performed incrementally. To allow accurate results to be obtained without the need of iteration, the stiffness equation of the domain is constructed by directly including a term related to the energy dissipation along the interface elements in the weak form of the global system equation. The constitutive law of cohesive cracks is then considered through this energy term. The validity and efficiency of the proposed method are shown by solving three numerical problems, *i.e.* the three-point bending test, the four-point single-notched shear test and the four-point double-notched shear test, all of plain concrete. The obtained results are compared with FE and experimental results reported in the literature.

2. THE EFG METHOD

Basically, the EFG method is different from FEM on how the shape functions are constructed. The construction of the shape functions in the EFG method is based on an approximation technique using the moving least square (MLS) method [11]. The MLS method is an effective technique for approximating a function using a set of scattered data. With the MLS technique, the approximation of a field increment $\Delta\phi(\mathbf{x})$ at any point $\mathbf{x}$ in a domain is expressed as

$$\Delta\phi(\mathbf{x}) = \sum_{j=1}^{m} p_j(\mathbf{x})\, a_j(\mathbf{x}) = \mathbf{p}^{\mathrm{T}}(\mathbf{x})\, \mathbf{a}(\mathbf{x}), \tag{1}$$

where $\mathbf{p}(\mathbf{x})$ is a vector containing a complete polynomial basis of arbitrary order. Here, m is the number of terms in the polynomial basis. In addition, $\mathbf{a}(\mathbf{x})$ is a vector of unknown coefficients. In this study, a linear basis function in two dimensions is used. Hence, $\mathbf{p}(\mathbf{x})$ and $\mathbf{a}(\mathbf{x})$ are, respectively, expressed as

$$\mathbf{p}^{\mathrm{T}}(\mathbf{x}) = [p_1(\mathbf{x}) \quad p_2(\mathbf{x}) \quad p_3(\mathbf{x})] = [1 \quad x \quad y], \tag{2}$$

$$\mathbf{a}^{\mathrm{T}}(\mathbf{x}) = [a_1(\mathbf{x}) \quad a_2(\mathbf{x}) \quad a_3(\mathbf{x})]. \tag{3}$$

Next, the values of the field increment at a set of nodes are used to construct a weighted squared error defined as

$$J = \sum_{I=1}^{n} w(\mathbf{x}-\mathbf{x}_I)\left[\mathbf{p}^{\mathrm{T}}(\mathbf{x}_I)\mathbf{a}(\mathbf{x}) - \Delta\phi_I\right]^2, \tag{4}$$

where $\Delta\phi_I$ and $\mathbf{x}_I$ are the nodal value of the field increment at node I and its position, respectively. In addition, $w(\mathbf{x}-\mathbf{x}_I)$ is a weight function that is centered at $\mathbf{x}_I$ and has a limit span. The weight function is defined as a non-negative monotonically decreasing function of the distance $d_I = |\mathbf{x}-\mathbf{x}_I|$. The neighborhood of node I where $w(\mathbf{x}-\mathbf{x}_I) \neq 0$ is called the domain of influence of node I. Also in the equation, n represents the number of nodes whose domains of influence contain $\mathbf{x}$.

The stationary of J in Eq. (4) with respect to $\mathbf{a}(\mathbf{x})$ yields

$$\mathbf{A}(\mathbf{x})\, \mathbf{a}(\mathbf{x}) = \mathbf{C}(\mathbf{x})\, \Delta\boldsymbol{\Phi}, \tag{5}$$

which can be solved for $\mathbf{a}(\mathbf{x})$ to yield

$$\mathbf{a}(\mathbf{x}) = \mathbf{A}^{-1}(\mathbf{x})\, \mathbf{C}(\mathbf{x})\, \Delta\boldsymbol{\Phi}, \tag{6}$$

where

$$\mathbf{A}(\mathbf{x}) = \sum_{I=1}^{n} w(\mathbf{x}-\mathbf{x}_I)\, \mathbf{p}(\mathbf{x}_I)\, \mathbf{p}^{\mathrm{T}}(\mathbf{x}_I), \tag{7}$$

$$\mathbf{C}(\mathbf{x}) = \left[w(\mathbf{x}-\mathbf{x}_1)\, \mathbf{p}(\mathbf{x}_1) \quad w(\mathbf{x}-\mathbf{x}_2)\, \mathbf{p}(\mathbf{x}_2) \quad \cdots \quad w(\mathbf{x}-\mathbf{x}_n)\, \mathbf{p}(\mathbf{x}_n)\right], \tag{8}$$

$$\Delta\boldsymbol{\Phi} = \left[\Delta\phi_1 \quad \Delta\phi_2 \quad \cdots \quad \Delta\phi_n\right]^{\mathrm{T}}. \tag{9}$$

By substituting Eq. (6) into Eq. (1), the field increment $\Delta\phi(\mathbf{x})$ is expressed as

$$\Delta\phi(\mathbf{x}) = \mathbf{p}^{\mathrm{T}}(\mathbf{x})\, \mathbf{A}^{-1}(\mathbf{x})\mathbf{C}(\mathbf{x})\, \Delta\boldsymbol{\Phi} = \mathbf{N}(\mathbf{x})\, \Delta\boldsymbol{\Phi}, \tag{10}$$

where the shape function matrix $\mathbf{N}(\mathbf{x})$ is defined as

$$\mathbf{N}(\mathbf{x}) = \mathbf{p}^{\mathrm{T}}(\mathbf{x})\,\mathbf{A}^{-1}(\mathbf{x})\,\mathbf{C}(\mathbf{x})\,. \tag{11}$$

In this paper, the Gaussian weight function employed by Belytschko and Fleming [21] is used to construct the weighted squared error in Eq. (4), *i.e.*,

$$w(d_I) = \begin{cases} \dfrac{e^{-(d_I/c)^2} - e^{-(d_{mI}/c)^2}}{1 - e^{-(d_{mI}/c)^2}} & d_I \le d_{mI} \\ 0 & d_I > d_{mI} \end{cases}, \tag{12}$$

where d_{mI} is the domain of influence of node I, and c is a parameter used to control the dilation of the weight function. It is important that appropriate values of d_{mI} and c are used in order that well formed shape functions are obtained. To achieve this, d_{mI} and c are defined as functions of nodal spacing through the use of another parameter called the characteristic nodal spacing c_I [21]. The parameter c_I is defined as a function of nodal spacing. Then, d_{mI} and c are written in terms of c_I as

$$d_{mI} = d_{\max} c_I\,, \tag{13}$$

$$c = \alpha c_I\,, \tag{14}$$

where $d_{\max}$ and α are constants. It is recommended that the ratio $d_{\max}/\alpha$ is not less than 4.0 in order to avoid poorly formed shape functions [21]. In this paper, $d_{\max}$ = 2.5 and α = 0.625 are used [21]. In addition, the characteristic nodal spacing c_I is chosen as the distance to the second nearest node for regularly spaced nodes and the distance to the third nearest node for irregularly spaced nodes [21].

3. MODELING OF COHESIVE CRACKS BY INTERFACE ELEMENTS

Consider a two-dimensional domain Ω in the xy plane with boundary Γ in Fig. 1(a). The boundary Γ is subdivided into two parts, *i.e.*, Γ_u where the displacement is prescribed, and Γ_t where the surface traction is prescribed. Assume further that there is a crack in the domain and it is represented as an additional boundary Γ_c inside Ω. The crack boundary Γ_c is composed of two opposite surfaces, *i.e.*, Γ_c^+ and Γ_c^-, as shown in Fig. 1(a). In this study, the crack is modeled by using connected straight-line interface elements as shown in Fig. 1(b). Each interface element contains the two surfaces of the crack. Figure 2(a) shows the i^{th} interface element and its local coordinate system whose origin is at the center of the element. The interface element has two coincident surfaces each of which has nodes at its ends. The two surfaces are designated as the positive surface ${}^i\Gamma_c^+$ and the negative surface ${}^i\Gamma_c^-$. When the crack opens, the two surfaces move away

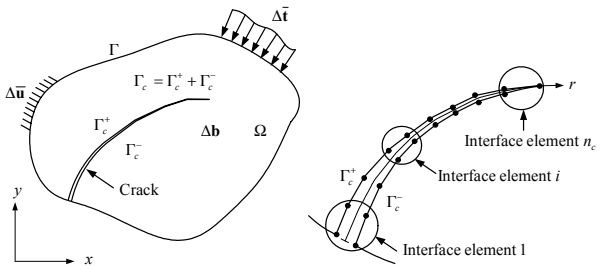

(b)

Fig. 1 Modeling of a crack by interface elements

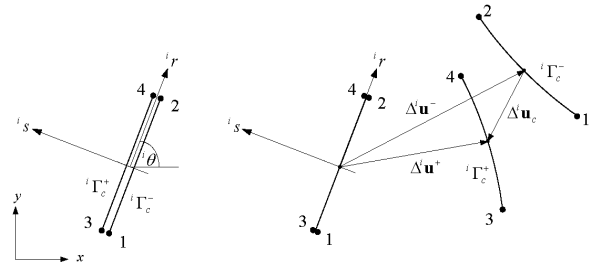

(a) (b)

Fig. 2 Details of the interface element

from each other. The crack displacement increment $\Delta^i\mathbf{u}_c$ along the length of the element in the global coordinate system shown in Fig. 2(b) is expressed as

$$\Delta^i\mathbf{u}_c({}^i r) = \begin{Bmatrix} \Delta^i u_c \\ \Delta^i v_c \end{Bmatrix} = \Delta^i\mathbf{u}^+({}^i r) - \Delta^i\mathbf{u}^-({}^i r)\,, \tag{15}$$

where $\Delta^i\mathbf{u}^+$ and $\Delta^i\mathbf{u}^-$ are the displacement increments along the positive and negative surfaces of the element, respectively. These two displacement increments $\Delta^i\mathbf{u}^+$ and $\Delta^i\mathbf{u}^-$ are expressed in terms of the nodal displacement increment $\Delta\mathbf{U}$ as

$$\Delta^i\mathbf{u}^+({}^i r) = \mathbf{N}[{}^i\mathbf{x}^+({}^i r)]\,\Delta\mathbf{U}\,, \tag{16}$$

$$\Delta^i\mathbf{u}^-({}^i r) = \mathbf{N}[{}^i\mathbf{x}^-({}^i r)]\,\Delta\mathbf{U}\,, \tag{17}$$

where

$$\mathbf{N}(\mathbf{x}) = \begin{bmatrix} N_1(\mathbf{x}) & 0 & \cdots & N_M(\mathbf{x}) & 0 \\ 0 & N_1(\mathbf{x}) & \cdots & 0 & N_M(\mathbf{x}) \end{bmatrix}, \tag{18}$$

$$\Delta\mathbf{U} = [\Delta u_1 \quad \Delta v_1 \quad \cdots \quad \Delta u_M \quad \Delta v_M]^{\mathrm{T}}\,. \tag{19}$$

Here, ${}^i\mathbf{x}^+$ and ${}^i\mathbf{x}^-$ represent two opposite points at position ${}^i r$ on the positive and negative surfaces, respectively. Note that the numerical values of ${}^i\mathbf{x}^+$ and ${}^i\mathbf{x}^-$ are in fact the same. However, two different symbols are

used to distinguish them. The subscript I in $N_I(\mathbf{x})$, Δu_I and Δv_I represent the node number while M represents the total number of nodes in the domain. The shape function matrices $\mathbf{N}[{}^i\mathbf{x}^+({}^ir)]$ and $\mathbf{N}[{}^i\mathbf{x}^-({}^ir)]$ are constructed by employing the method described in the previous section. However, during the construction of the matrices, the domains of influence of nodes are considered based on the visibility criterion [17]. The visibility criterion is necessary for constructing shape functions near a crack. The concept of this criterion is that the domain boundaries and any lines of cracks are treated as opaque objects during the construction of weight functions. In Fig. 3(a), consider node I that has a crack line within its domain of influence. The radius d_{mI}, which is used to determine the domain of influence of node I, is treated as a ray of light. When the ray encounters the opaque crack line, it is terminated and the area that is not reached by the ray is excluded from the domain of influence of node I. As a result, in Fig. 3(a), the shaded region becomes the modified domain of influence of node I. In consequence of the visibility criterion, nodes that are used in the approximation of $\Delta^i\mathbf{u}^+({}^ir)$ and $\Delta^i\mathbf{u}^-({}^ir)$ will be different as schematically shown in Fig. 3(b). This difference can be seen in the difference between $\mathbf{N}[{}^i\mathbf{x}^+({}^ir)]$ and $\mathbf{N}[{}^i\mathbf{x}^-({}^ir)]$.

By substituting Eqs. (16) and (17) into Eq. (15), the crack displacement increment $\Delta^i\mathbf{u}_c$ is written as

$$\Delta^i\mathbf{u}_c({}^ir)=\left(\mathbf{N}[{}^i\mathbf{x}^+({}^ir)]-\mathbf{N}[{}^i\mathbf{x}^-({}^ir)]\right)\Delta\mathbf{U}={}^i\mathbf{N}_c({}^ir)\Delta\mathbf{U} \quad (20)$$

where ${}^i\mathbf{N}_c({}^ir)$ is the crack shape function matrix defined as

$${}^i\mathbf{N}_c({}^ir)=\mathbf{N}[{}^i\mathbf{x}^+({}^ir)]-\mathbf{N}[{}^i\mathbf{x}^-({}^ir)]. \quad (21)$$

Constitutive laws for cohesive cracks are normally described with respect to local coordinate systems of the cracks. Therefore, the crack displacement increment $\Delta^i\hat{\mathbf{u}}_c$ in the local ${}^ir-{}^is$ coordinate system must be introduced, *i.e.*,

$$\Delta^i\hat{\mathbf{u}}_c({}^ir)=\begin{Bmatrix}\Delta^i\hat{u}_c({}^ir)\\ \Delta^i\hat{v}_c({}^ir)\end{Bmatrix}={}^i\hat{\mathbf{T}}\Delta^i\mathbf{u}_c({}^ir), \quad (22)$$

where $\Delta^i\hat{u}_c$ and $\Delta^i\hat{v}_c$ represent the crack sliding and opening displacement increments, respectively. In addition, ${}^i\hat{\mathbf{T}}$ is the transformation matrix defined as

$${}^i\hat{\mathbf{T}}=\begin{bmatrix}\cos({}^i\theta) & \sin({}^i\theta)\\ -\sin({}^i\theta) & \cos({}^i\theta)\end{bmatrix}. \quad (23)$$

Here, ${}^i\theta$ is the angle between the local ${}^ir$ axis and the global x axis as shown in Fig. 2(a).

Write the transmitted crack traction increment $\Delta^i\hat{\mathbf{t}}_c$ in the local coordinate system as

$$\Delta^i\hat{\mathbf{t}}_c=\begin{Bmatrix}\Delta^i\hat{t}_r\\ \Delta^i\hat{t}_s\end{Bmatrix}. \quad (24)$$

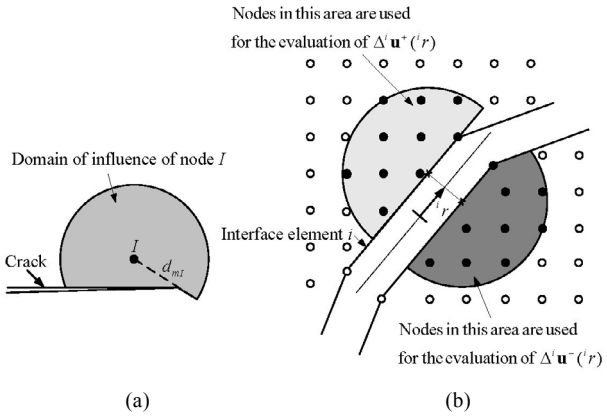

Fig. 3 Domain of influence near a crack

Here, $\Delta^i\hat{\mathbf{t}}_c$ is defined as the traction increment exerted by the positive surface onto the negative surface of the interface element.

Next, the crack constitutive law is introduced as

$$\Delta^i\hat{\mathbf{t}}_c({}^ir)=\hat{\mathbf{D}}_c\,\Delta^i\hat{\mathbf{u}}_c({}^ir), \quad (25)$$

where $\hat{\mathbf{D}}_c$ is the crack constitutive matrix defined as

$$\hat{\mathbf{D}}_c=\begin{bmatrix}D^{II} & 0\\ 0 & D^I\end{bmatrix}, \quad (26)$$

where D^I and D^{II} represent the mode I and mode II crack moduli, respectively. Note that D^I and D^{II} are functions of the crack opening and sliding displacements.

By employing Eqs. (20), (22) and (25), the local crack displacement increment $\Delta^i\hat{\mathbf{u}}_c$ and local crack traction increment $\Delta^i\hat{\mathbf{t}}_c$ are written in terms of the nodal displacement increment $\Delta\mathbf{U}$ as

$$\Delta^i\hat{\mathbf{u}}_c({}^ir)={}^i\hat{\mathbf{T}}\,{}^i\mathbf{N}_c({}^ir)\Delta\mathbf{U}, \quad (27)$$

$$\Delta^i\hat{\mathbf{t}}_c({}^ir)=\hat{\mathbf{D}}_c\,{}^i\hat{\mathbf{T}}\,{}^i\mathbf{N}_c({}^ir)\Delta\mathbf{U}. \quad (28)$$

In this study, to simulate crack growth, the existing crack is lengthened, in each incremental step, by extending the crack line using a new interface element. The extension of the crack is assumed to be of mode I. Therefore, the extension occurs when the maximum principal tensile stress ahead of the crack tip reaches the value of the tensile strength of the material. The direction of the extension is set to be perpendicular to the direction of this maximum principal tensile stress.

4. DERIVATION OF THE STIFFNESS MATRIX EQUATION

The weak form of the problem can be written as

$$\left[\int_{\Omega}\delta(\Delta\boldsymbol{\varepsilon}^{\mathrm{T}})\Delta\boldsymbol{\sigma}d\Omega-\int_{\Omega}\delta(\Delta\mathbf{u}^{\mathrm{T}})\Delta\mathbf{b}d\Omega-\int_{\Gamma_t}\delta(\Delta\mathbf{u}^{\mathrm{T}})\Delta\bar{\mathbf{t}}d\Gamma-\int_{\Gamma_u}\delta(\Delta\boldsymbol{\lambda}^{\mathrm{T}})(\Delta\mathbf{u}-\Delta\bar{\mathbf{u}})d\Gamma-\int_{\Gamma_u}\delta(\Delta\mathbf{u}^{\mathrm{T}})\Delta\boldsymbol{\lambda}d\Gamma\right]+\left[\sum_{i=1}^{n_c}\int_{{}^{i}\Gamma_c^-}\delta(\Delta^{i}\hat{\mathbf{u}}_c^{\mathrm{T}})\Delta^{i}\hat{\mathbf{t}}_c d\Gamma\right]=0\,. \tag{29}$$

The above weak form consists of two parts. The terms in the first brackets are the well-known terms found in the weak form for the EFG method which requires the use of Lagrange multipliers to enforce the essential boundary conditions [10]. Here, $\Delta\boldsymbol{\lambda}$ denotes a vector containing Lagrange multiplier increments defined as

$$\Delta\boldsymbol{\lambda}=\begin{Bmatrix}\Delta\lambda_x\\ \Delta\lambda_y\end{Bmatrix}. \tag{30}$$

The term in the second brackets is associated to the energy dissipation from the cohesive crack which is modeled by n_c interface elements. The other symbols are either mentioned earlier or self-evident.

In this study, the constitutive law of the material is assumed to be linear elastic, *i.e.*,

$$\Delta\boldsymbol{\sigma}=\mathbf{D}\Delta\boldsymbol{\varepsilon}\,, \tag{31}$$

where $\mathbf{D}$ is the constitutive matrix. By employing the EFG shape functions constructed by the methods explained in the previous sections, the displacement increment $\Delta\mathbf{u}$ and the strain increment $\Delta\boldsymbol{\varepsilon}$ are written in terms of the nodal displacement increment $\Delta\mathbf{U}$ as

$$\Delta\mathbf{u}=\mathbf{N}\Delta\mathbf{U}\,, \tag{32}$$

$$\Delta\boldsymbol{\varepsilon}=\mathbf{B}\Delta\mathbf{U}\,, \tag{33}$$

where $\mathbf{N}$ and $\mathbf{B}$ represent the shape function matrix and its derivative matrix, respectively.

The Lagrange multiplier increment $\Delta\boldsymbol{\lambda}$ is interpolated from its nodal values by using Lagrange interpolation as

$$\Delta\boldsymbol{\lambda}(\mathbf{x})=\mathbf{N}_{\lambda}(r_u)\Delta\boldsymbol{\Lambda}\qquad\mathbf{x}\in\Gamma_u\,, \tag{34}$$

where $\mathbf{N}_{\lambda}(r_u)$ is a Lagrange-interpolant matrix and r_u denotes the arc length along the boundary Γ_u. In addition, $\Delta\boldsymbol{\Lambda}$ is a vector containing nodal Lagrange multiplier increments of all the nodes on the boundary Γ_u.

By substituting Eqs. (27)-(28) and Eqs. (31)-(34) into Eq. (29), the weak form becomes

$$\begin{bmatrix}\delta(\Delta\mathbf{U}^{\mathrm{T}})\int_{\Omega}\mathbf{B}^{\mathrm{T}}\mathbf{D}\mathbf{B}d\Omega\Delta\mathbf{U}-\delta(\Delta\mathbf{U}^{\mathrm{T}})\int_{\Omega}\mathbf{N}^{\mathrm{T}}\Delta\mathbf{b}d\Omega\\ -\delta(\Delta\mathbf{U}^{\mathrm{T}})\int_{\Gamma_t}\mathbf{N}^{\mathrm{T}}\Delta\bar{\mathbf{t}}d\Gamma-\delta(\Delta\boldsymbol{\Lambda}^{\mathrm{T}})\int_{\Gamma_u}\mathbf{N}_{\lambda}^{\mathrm{T}}\mathbf{N}d\Gamma\Delta\mathbf{U}\\ +\delta(\Delta\boldsymbol{\Lambda}^{\mathrm{T}})\int_{\Gamma_u}\mathbf{N}_{\lambda}^{\mathrm{T}}\Delta\bar{\mathbf{u}}d\Gamma-\delta(\Delta\mathbf{U}^{\mathrm{T}})\int_{\Gamma_u}\mathbf{N}^{\mathrm{T}}\mathbf{N}_{\lambda}d\Gamma\Delta\boldsymbol{\Lambda}\end{bmatrix}+\left[\delta(\Delta\mathbf{U}^{\mathrm{T}})\sum_{i=1}^{n_c}\int_{{}^{i}\Gamma_c^-}{}^{i}\mathbf{N}_c^{\mathrm{T}}\,{}^{i}\hat{\mathbf{T}}^{\mathrm{T}}\hat{\mathbf{D}}_c\,{}^{i}\hat{\mathbf{T}}\,{}^{i}\mathbf{N}_c d\Gamma\Delta\mathbf{U}\right]=0\,. \tag{35}$$

Finally, since $\delta(\Delta\mathbf{U}^{\mathrm{T}})$ and $\delta(\Delta\boldsymbol{\Lambda}^{\mathrm{T}})$ are arbitrary, the stiffness equation is written as

$$\begin{bmatrix}\mathbf{K}&\mathbf{G}\\ \mathbf{G}^{T}&0\end{bmatrix}\begin{Bmatrix}\Delta\mathbf{U}\\ \Delta\boldsymbol{\Lambda}\end{Bmatrix}=\begin{Bmatrix}\Delta\mathbf{R}_1\\ \Delta\mathbf{R}_2\end{Bmatrix}, \tag{36}$$

where

$$\mathbf{K}=\int_{\Omega}\mathbf{B}^{\mathrm{T}}\mathbf{D}\mathbf{B}d\Omega+\sum_{i=1}^{n_c}\int_{{}^{i}\Gamma_c^-}{}^{i}\mathbf{N}_c^{\mathrm{T}}\,{}^{i}\hat{\mathbf{T}}^{\mathrm{T}}\hat{\mathbf{D}}_c\,{}^{i}\hat{\mathbf{T}}\,{}^{i}\mathbf{N}_c d\Gamma\,, \tag{37}$$

$$\mathbf{G}=-\int_{\Gamma_u}\mathbf{N}^{\mathrm{T}}\mathbf{N}_{\lambda}d\Gamma\,, \tag{38}$$

$$\Delta\mathbf{R}_1=\int_{\Omega}\mathbf{N}^{\mathrm{T}}\Delta\mathbf{b}d\Omega+\int_{\Gamma_t}\mathbf{N}^{\mathrm{T}}\Delta\bar{\mathbf{t}}d\Gamma\,, \tag{39}$$

$$\Delta\mathbf{R}_2=-\int_{\Gamma_u}\mathbf{N}_{\lambda}^{\mathrm{T}}\Delta\bar{\mathbf{u}}d\Gamma\,. \tag{40}$$

5. RESULTS

The validity and efficiency of the proposed method are shown by solving three numerical problems. They are the three-point bending test, the four-point single-notched shear test, and the four-point double-notched shear test, all of plain concrete. The shear fracture resistance is neglected in this study. The three tests are analyzed with three different types of tension softening curve, *i.e.*, the linear softening curve [1], bilinear softening curve [2], and exponential softening curve [4]. The three tension softening curves are shown in Fig. 4. For the four-point single-notched shear test, besides three different types of tension-softening curve, two sets of material properties are used in order that comparison with two different existing works is possible. The details of the material properties used in all problems are shown in Table 1.

5.1 Three-Point Bending Test

The most commonly used configuration to investigate the mode I crack propagation in concrete is a notched beam subjected to three-point bending. In this study, the beam shown in Fig. 5 is used. The depth, length and thickness of the beam are 100mm, 510mm and 100mm, respectively. The ratio between the notched depth and the beam depth is equal to 0.5. The crack mount opening displacement (CMOD) is used as a controlling parameter of loading. Figure 6 shows the mesh of nodes of the problem that consists of 313 nodes.

The obtained results are compared with a result from FE analysis by Prasad and Krishnamoorthy [4] and experimental results by Körmeling and Reinhardt [31] as shown in Fig. 7. It is found that the obtained responses are in good agreement with the FE and experimental results. Nevertheless, the results obtained with the bilinear and exponential tension-softening curves agree better with the experimental results. The result

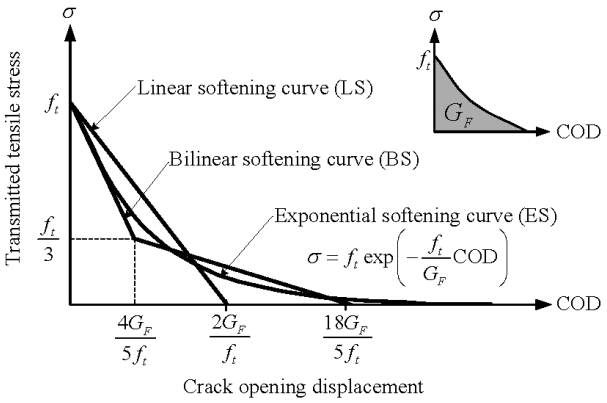

Fig. 4 Tension-softening curves

Table 1 Material properties

Problem	Parameter Set	E (GPa)	v	f_t (MPa)	G_F (N/m)	Softening Curve
Three-point bending test	LS	20.0	0.20	2.40	113.0	Linear
	BS					Bilinear
	ES					Exponential
Four-point single-notched shear test	LS-A	24.8	0.18	2.80	100.0	Linear
	BS-A					Bilinear
	ES-A					Exponential
	LS-B	30.0	0.20	3.33	124.0	Linear
	BS-B					Bilinear
	ES-B					Exponential
Four-point double-notched shear test	LS	27.0	0.10	2.00	100.0	Linear
	BS					Bilinear
	ES					Exponential

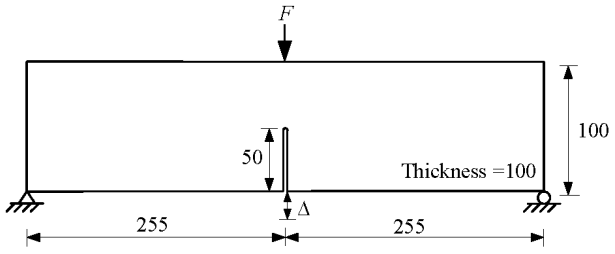

Fig. 5 Three-point bending beam (unit: mm)

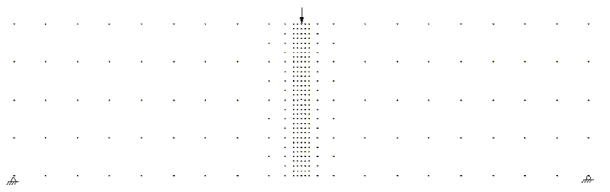

Fig. 6 Mesh of nodes for the three-point bending beam

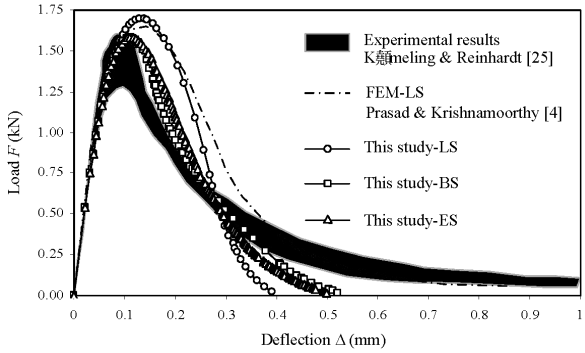

Fig. 7 Load-deflection responses of the three-point bending beam

obtained with the linear tension-softening curve agrees closely with the result by Prasad and Krishnamoorthy [4] which is also obtained with the linear tension-softening curve. However, it can be seen that the discrepancy between the two results increases with the increased deflection. Since the same material properties and mechanical assumptions are used to obtain the two results, this discrepancy is due to the difference in the approximation methods employed. The discrepancy actually becomes larger in the later incremental steps. This is because of the nature of the incremental analysis. In the incremental analysis of crack propagation, there is a general tendency that the error will be accumulated during each incremental step. Thus, any difference between different incremental models will become more pronounced in the later steps. The results obtained with the bilinear and exponential tension-softening curves are expected to have lower peak loads than those obtained with the linear tension-softening curve. This is because the bilinear and exponential tension-softening curves have steeper initial slopes than that of the linear curve. A steeper initial slope means that the material is initially more brittle. Figure 8 shows the deformed shapes of the beam from the peak load for the case analyzed with the exponential tension-softening curve.

5.2 Four-Point Single-Notched Shear Test

The second numerical example is the four-point single-notched shear test. In this study, the beam shown in Fig. 9 is employed. The depth, length and thickness of the beam are 306mm, 914mm and 156mm, respectively. In this problem, the crack mount sliding displacement (CMSD) is used as a controlling parameter of loading. Besides three different types of tension softening curve, two sets of material properties are employed and they are designated as material sets A and B. Material set A is used in FE analysis by Alfaiate *et al.* [2] while material set B is used in FE analysis by Prasad and Krishnamoorthy [4]. Figure 10 shows the mesh of nodes of the problem that consists of 2,412 nodes. It can be seen from the figure that more nodes are added around the notch tip. This is to cope with the initial crack direction that is quite different from the direction of the notch.

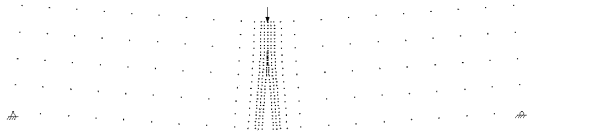

(a) F = 1.58kN (peak load)

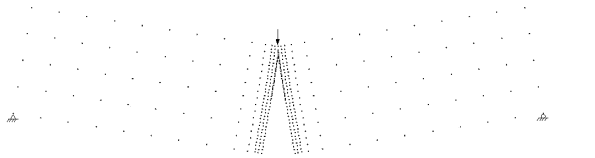

(b) F = 0.74kN (postpeak load)

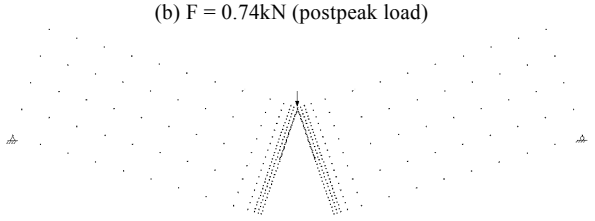

(c) F = 0.02kN (postpeak load)

Fig. 8 Deformed shape of the three-point bending beam from the peak load

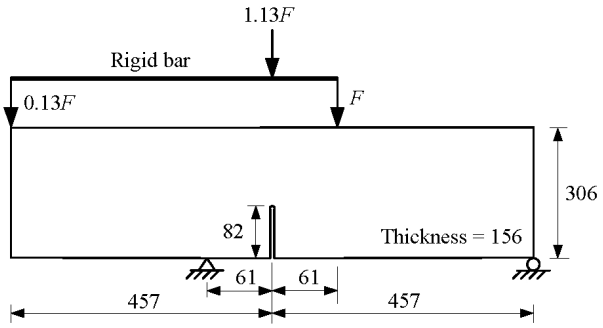

Fig. 9 Four-point single-notched shear beam (unit: mm)

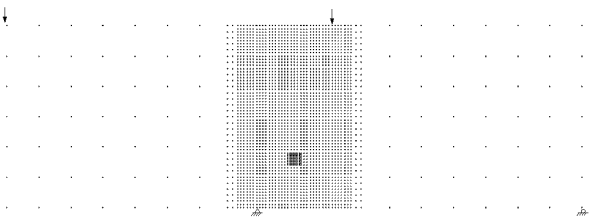

Fig. 10 Mesh of nodes for the four-point single-notched shear beam

The obtained results are compared with the FE results by Alfaiate *et al.* [2] and by Prasad and Krishnamoorthy [4]. Note that Alfaiate *et al.* [2] use the bilinear tension-softening curve in their analysis while Prasad and Krishnamoorthy [4] use the linear tension-softening curve. The comparison is shown in Fig. 11. It is found from the comparison that the obtained responses are in good agreement with the results by Alfaiate *et al*. [2] and by Prasad and Krishnamoorthy [4], when the responses with the same types of the tension-softening curve are considered. As expected, the results obtained with the bilinear and exponential softening curves have lower peak loads than those obtained with the linear tension-softening curve. The obtained crack paths are compared with those reported by Alfaiate *et al.* [2] and by Prasad and Krishnamoorthy [4] in Fig. 12. All of the crack paths agree very well. Figure 13 shows the deformed shapes of the beam from the peak load for the case analyzed with material set A and the exponential tension-softening curve.

5.3 Four-Point Double-Notched Shear Test

The last numerical example is the four-point double-notched shear test. The geometry of the tested beam

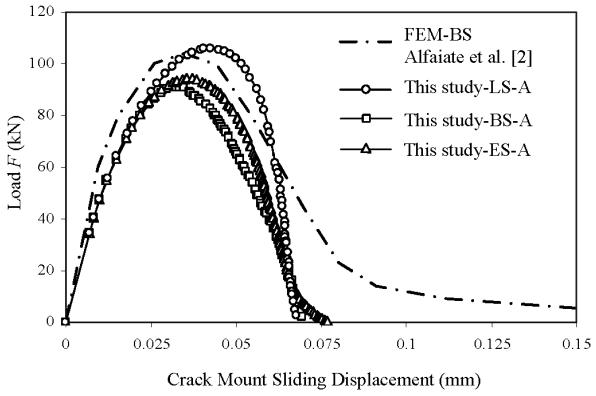

(a)

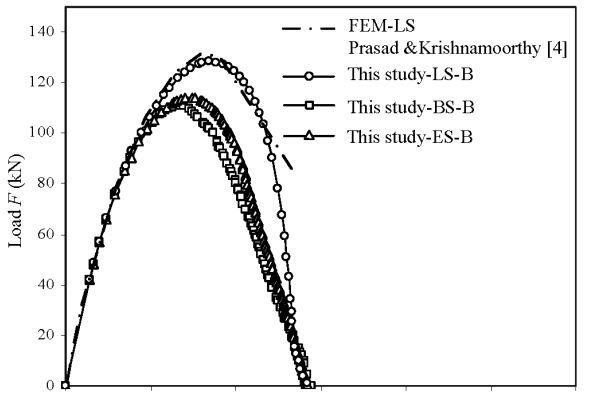

(b)

Fig. 11 Load-CMSD responses of the four-point single-notched shear beam

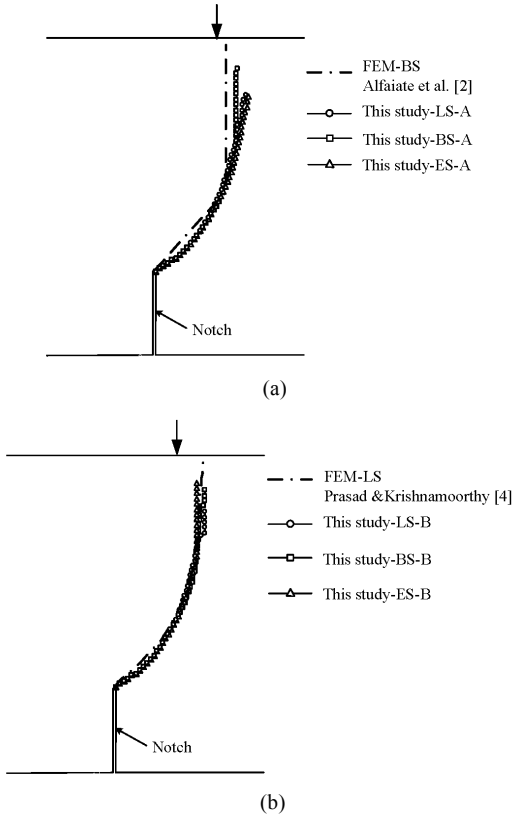

Fig. 12 Crack paths of the four-point single-notched shear beam

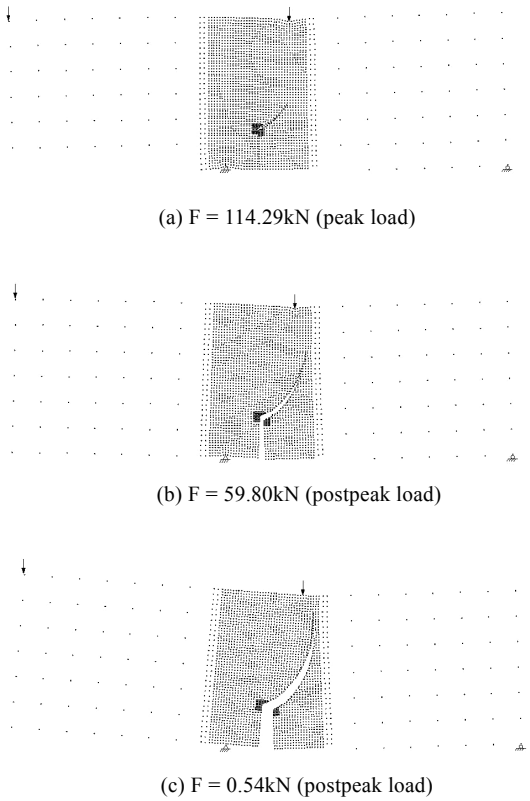

Fig. 13 Deformed shape of the four-point single-notched shear beam from the peak load

and the boundary conditions are shown in Fig. 14. The depth, length and thickness of the beam are 200mm, 800mm and 100mm, respectively. In this problem, the crack mount sliding displacement (CMSD) is used as a controlling parameter of loading. Figure 15 shows the mesh of nodes of the problem that consists of 1,899 nodes.

The obtained results are compared with FE and experimental results by Bocca *et al.* [1] as shown in Fig. 16. In general, good agreements between the obtained results and the FE and experimental results can be observed. However, the results from the proposed method with the bilinear and exponential softening curves seem to agree better with the experimental result. The FE result by Bocca *et al.* [1] which is obtained with the linear tension-softening curve is found to have a higher peak load than those of the experimental result and the proposed result with the same type of the tension-softening curve. Nevertheless, its postpeak response agrees well with the experimental result as well as the proposed results obtained with the bilinear and exponential tension-softening curves. In Fig. 17, the crack paths are presented. All of the crack paths agree very well. Figure 18 shows the deformed shapes of the beam from the peak load for the case analyzed with the exponential tension-softening curve.

6. CONCLUSIONS

This paper presents the application of the EFG method for analysis of cohesive crack growth in 2D domains. Interface elements are used in the model to represent displacement discontinuities due to cracks. A curved crack is simply represented by connected straight-line interface elements. To simulate crack growth, the existing crack is lengthened in each incremental step by extending the crack line using an interface element. The interface elements permit the constitutive law of cohesive cracks to be considered directly and efficiently. The relative displacement increments between the two opposite surfaces of the interface elements are the crack displacement increments. The crack displacement increments are written in terms of the nodal displacement increments by using the EFG shape functions that employ the visibility criterion. To allow accurate analysis to be performed without the need of iteration, the stiffness equation of the domain is constructed by directly including a term related to the energy dissipation along the interface elements in the EFG weak form of the global system equation. If this energy term is not directly included in the derivation, the cohesive stresses on the crack surfaces will have to be treated as applied surface tractions. Subsequently, their magnitudes will have to be determined via iterations. The interface elements and the EFG method allow a crack to propagate without any constraint on its direction and without remeshing. The analysis of example problems taken from the literature clearly shows

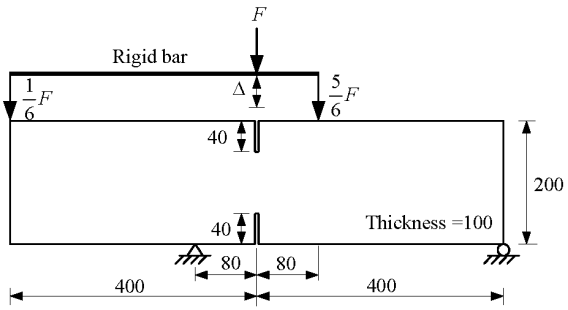

Fig. 14 Four-point double-notched shear beam (unit: mm)

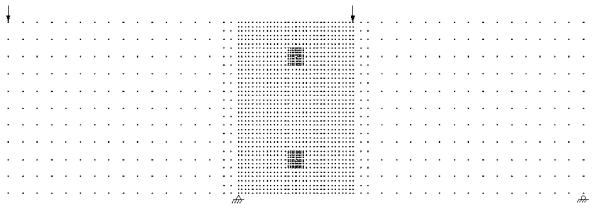

Fig. 15 Mesh of nodes for the four-point double-notched shear beam

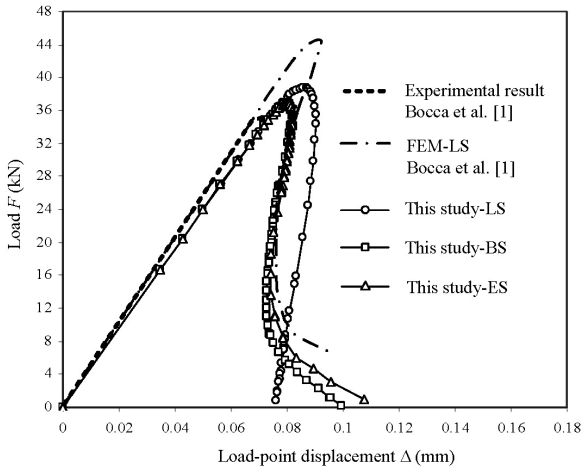

Fig. 16 Load-displacement responses of the four-point double-notched shear beam

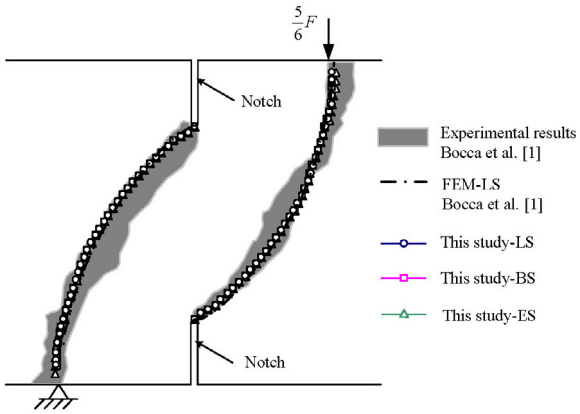

Fig. 17 Crack paths of the four-point double-notched shear beam

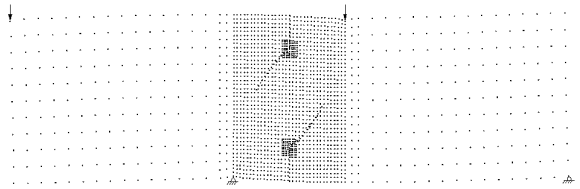

(a) F = 36.92kN (peak load)

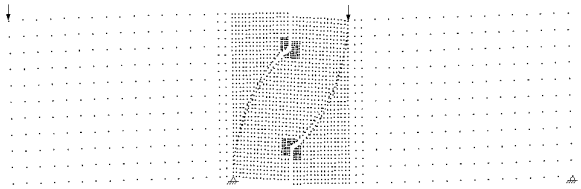

(b) F = 23.69kN (postpeak load)

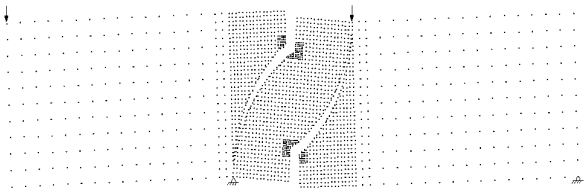

(c) F = 1.04kN (postpeak load)

Fig. 18 Deformed shape of the four-point double-notched shear beam from the peak load

the validity and efficiency of the proposed method. The results of the proposed method are found to be in good agreement with the FE and experimental results from the literature. It can reasonably be concluded that the use of the interface elements in conjunction with the EFG method is an efficient way for simulating propagation of cohesive cracks.

REFERENCES

1. Bocca, P., Carpinteri, A. and Valente, S., "Mixed Mode Fracture of Concrete," *International Journal of Solids and Structures*, 27, pp. 1139–1153 (1991).
2. Alfaiate, J., Pires, E. B. and Martins, J. A. C., "A Finite Element Analysis of Non-Prescribed Crack Propagation in Concrete," *Computers & Structures*, 63, pp. 17–26 (1997).
3. Moës, N. and Belytschko, T., "Extended Finite Element Method for Cohesive Crack Growth," *Engineering Fracture Mechanics*, 69, pp. 813–833 (2002).
4. Prasad, M. V. K. V. and Krishnamoorthy, C. S., "Computational Model for Discrete Crack Growth in Plain and Reinforced Concrete," *Computer Methods in Applied Mechanics and Engineering*, 191, pp. 2699–2725 (2002).
5. Gálvez, J. C., Červenka, J., Cendón, D. A. and Saouma, V., "A Discrete Crack Approach to Normal/Shear Cracking of Concrete," *Cement and Concrete Research*,

32, pp. 1567–1585 (2002).
6. Yang, Z. and Chen, J., "Fully Automatic Modelling of Cohesive Discrete Crack Propagation in Concrete Beams Using Local Arc-Length Methods," *International Journal of Solids and Structures*, 41, p. 801 (2004).
7. Dvorkin, E. N. and Assanelli, A. P., "2D Finite Elements with Displacement Interpolated Embedded Localization Lines — The Analysis of Fracture in Frictional Materials," *Computer Methods in Applied Mechanics and Engineering*, 90, pp. 829–844 (1991).
8. Wells, G. N. and Sluys, L. J., "Three-Dimensional Embedded Discontinuity Model for Brittle Fracture," *International Journal of Solids and Structures*, 38, pp. 897–913 (2001).
9. Alfaiate, J., Wells, G. N. and Sluys, L. J., "On the Use of Embedded Discontinuity Elements with Crack Path Continuity for Mode-I and Mixed-Mode Fracture," *Engineering Fracture Mechanics*, 69, pp. 661–686 (2002).
10. Belytschko, T., Lu, Y. Y. and Gu, L., "Element-Free Galerkin Methods," *International Journal for Numerical Methods in Engineering*, 37, pp. 229–256 (1994).
11. Lancaster, P. and Salkauskas, K., "Surfaces Generated by Moving Least Squares Methods," *Mathematics of Computation*, 37, pp. 141–158 (1981).
12. Chyuan, S. W. and Lin, J.-H., "Dual Boundary Element Analysis for Fatigue Behavior of Missile Structures," *Journal of the Chinese Institute of Engineers,* 23, pp. 339–348 (2000).
13. Chen, J. T. and Hong, H. K., "Review of Dual Boundary Element Methods with Emphasis on Hypersingular Integrals and Divergent Series," *Applied Mechanics Reviews*, 52, pp. 17–32 (1999).
14. Armentani, E. and Citarella, R., "DBEM and FEM Analysis on Non-Linear Multiple Crack Propagation in an Aeronautic Doubler-Skin Assembly," *International Journal of Fatigue*, 28, pp. 598–608 (2006).
15. Aour, B., Rahmani, O. and Nait-Abdelaziz, M., "A Coupled FEM/BEM Approach and Its Accuracy for Solving Crack Problems in Fracture Mechanics," *International Journal of Solids and Structures*, 44, pp. 2523–2539 (2007).
16. Yan, X., "Numerical Analysis of a Few Complex Crack Problems with a Boundary Element Method," *Engineering Failure Analysis*, 13, pp. 805–825 (2006).
17. Belytschko, T., Krongauz, Y., Organ, D., Fleming, M. and Krysl, P., "Meshless Methods: An Overview and Recent Developments," *Computer Methods in Applied Mechanics and Engineering*, 139, pp. 3–47 (1996).
18. Belytschko, T., Lu, Y. Y. and Gu, L., "Crack Propagation by Element-Free Galerkin Methods," *Engineering Fracture Mechanics*, 51, pp. 295–315 (1995).
19. Belytschko, T., Lu, Y. Y., Gu, L. and Tabbara, M., "Element-Free Galerkin Methods for Static and Dynamic Fracture," *International Journal of Solids and Structures*, 32, pp. 2547–2570 (1995).
20. Belytschko, T. and Tabbara, M., "Dynamic Fracture Using Element-Free Galerkin Methods," *International Journal for Numerical Methods in Engineering*, 39, pp. 923–938 (1996).
21. Belytschko, T. and Fleming, M., "Smoothing, Enrichment and Contact in the Element-Free Galerkin Method," *Computers and Structures*, 71, pp. 173–195 (1999).
22. Krysl, P. and Belytschko, T., "The Element Free Galerkin Method for Dynamic Propagation of Arbitrary 3-D Cracks," *International Journal for Numerical Methods in Engineering*, 44, pp. 767–800 (1999).
23. Rao, B. N. and Rahman, S., "An Efficient Meshless Method for Fracture Analysis of Cracks," *Computational Mechanics*, 26, pp. 398–408 (2000).
24. Lee, S. H. and Yoon, Y. C., "Numerical Prediction of Crack Propagation by an Enhanced Element-Free Galerkin Method," *Nuclear Engineering and Design*, 227, pp. 257–271 (2004).
25. Xu, Y. and Saigal, S., "An Element Free Galerkin Formulation for Stable Crack Growth in an Elastic Solid," *Computer Methods in Applied Mechanics and Engineering*, 154, pp. 331–343 (1998).
26. Häussler-Combe, U. and Korn, C., "An Adaptive Approach with the Element-Free-Galerkin Method," *Computer Methods in Applied Mechanics and Engineering*, 162, pp. 203–222 (1998).
27. Xu, Y. and Saigal, S., "An Element Free Galerkin Analysis of Steady Dynamic Growth of a Mode I Crack in Elastic-Plastic Materials," *International Journal of Solids and Structures*, 36, pp. 1045–1079 (1999).
28. Shen, K. J., Sheng, J. P. and Wang, C. Y., "Study of Static Fracture Propagation by Element-Free Galerkin Method with Singular Weight Function at Crack Tip," *Journal of Mechanics*, 21, pp. 125–129 (2005).
29. Hillerborg, A., Modeer, M. and Petersson, P. E., "Analysis of Crack Formation and Crack Growth in Concrete by Means of Fracture Mechanics and Finite Elements," *Cement and Concrete Research*, 6, pp. 773–781 (1976).
30. Belytschko, T., Organ, D. and Gerlach, C., "Element-Free Galerkin Methods for Dynamic Fracture in Concrete," *Computer Methods in Applied Mechanics and Engineering*, 187, pp. 385–399 (2000).
31. Körmeling, H. A. and Reinhardt, H. W., "Determination of the Fracture Energy of Normal Concrete and Epoxy Modified Concrete, Report No. 5-83-18," Delft University of Technology, Delft (1983).

(Manuscript received January 15, 2007,
accepted for publication March 30, 2007.)